

Polar-Drive Experiments with Shimmed Targets on OMEGA

The polar-drive (PD) approach to directly driven, inertial confinement fusion¹ is being pursued as a means of demonstrating thermonuclear ignition at the National Ignition Facility² (NIF) with the beams of NIF in the indirect-drive configuration. Extensive experiments have been performed on the OMEGA Laser System³ to evaluate this technique.^{4–7} Ignition target designs using cryogenically cooled, DT-filled CH shells have been investigated using two-dimensional (2-D) hydrodynamic simulations.^{8,9} These simulations suggest that gains of at least 20 to 30 can be achieved using 1.5 MJ of laser energy to irradiate a DT-ice-layer-bearing cryogenic target. In a recent simulation study by Collins *et al.*,⁹ the drive symmetry was optimized by using a combination of beam pointing, beam shaping, pulse shaping, and target-layer shimming. Shimming uses an ideal ice-layer profile that is thinner at the target equator, where the beam illumination is the most oblique, and energy coupling to the target is reduced. The inclusion of an ice-layer shim increased the gain of the ignited plasma. Collins *et al.* also note that a shim applied to the CH capsule could equivalently be used to shape the imploding plasma.⁹ This article presents the first results of shimmed PD experiments showing that improved implosion symmetry is obtained. The experiments were performed on the OMEGA Laser System in the PD configuration with D₂-gas-filled, shimmed CH shells.

The unablated shell material in a laser-driven implosion behaves much like the payload of a rocket.¹⁰ The final velocity of the unablated shell depends nonlinearly on the initial shell thickness and the intensity of the laser light being used to accelerate the shell through ablation.¹⁰ For polar drive, the intensity varies as a function of both polar angle and time. Optimizing polar drive is accomplished by picking the beam shapes, beam pointing, pulse shapes, and target-shim profile that result in the most spherically shaped implosion, leading to the highest target gain. This is done experimentally and with simulations using a 2-D hydrodynamics code. If it is assumed that lateral mass flow in the imploding shell can be neglected, then the simulations can be performed with a one-dimensional (1-D) hydrocode, provided that the amount of absorbed energy can be accurately predicted. To apply this to polar drive it is

assumed that the average absorbed intensity is solely a function of polar angle. The capsule thickness as a function of polar angle needed to compensate for the angular variation of the average intensity can therefore be determined from a series of 1-D simulations. This is illustrated in Fig. 135.12, where the calculated trajectories of the fuel–shell interface R_{fs} as a function of time for two D₂-filled CH shells with identical inner shell radii (412 μm) and fill pressure (10 atm), but with differing shell thicknesses of 24 and 27 μm , respectively, are shown. The simulations were performed with the 1-D hydrocode *LILAC*¹¹ for nominal laser conditions of 27 kJ of UV light in a 1-ns square pulse ($\sim 1 \times 10^{15}$ W/cm² at a radius of 430 μm). The 27- μm shell implodes more slowly than the 24- μm shell. R_{fs} is also shown for an intensity reduced to 80% of the nominal case. This trajectory (dashed line) is nearly identical to that of the 27- μm -thick shell at the nominal intensity.

A series of such simulations were performed to determine the approximate shell thickness as a function of average intensity needed so that R_{fs} was the same as the nominal intensity case at a time close to shell stagnation. Figure 135.13 shows

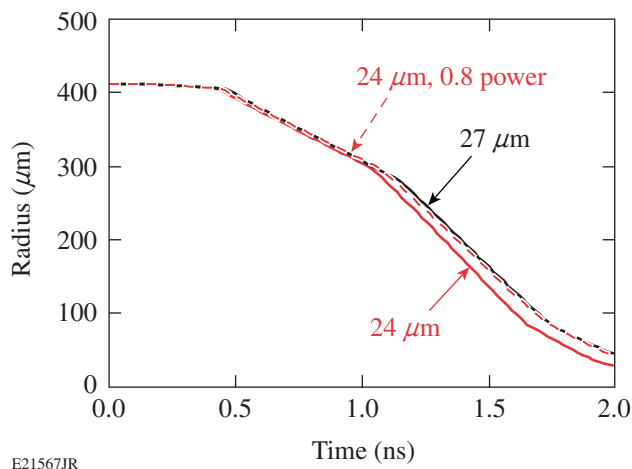
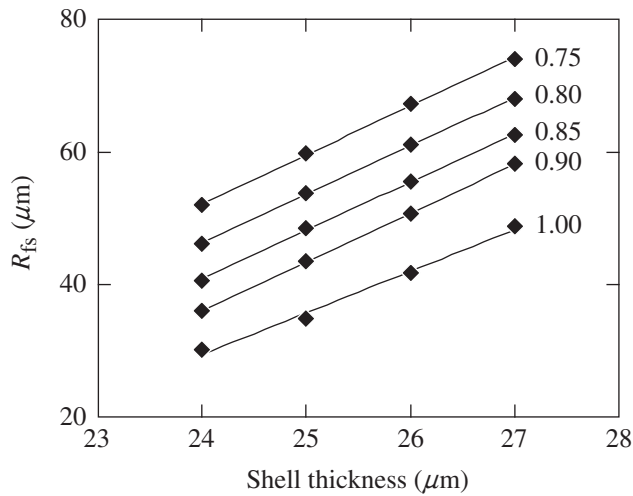


Figure 135.12
Simulated fuel–shell interface R_{fs} trajectory for a 24- and a 27- μm -thick shell at nominal laser conditions of 27 kJ, 1-ns square pulse, and for a 24- μm -thick shell at 0.8 times nominal laser intensity.



E21812JR

Figure 135.13

Simulated values of R_{fs} at $t = 2.0$ ns as a function of shell thickness for cases of 0.75, 0.80, 0.85, 0.90, and 1.00 times nominal laser intensity.

values of R_{fs} at $t = 2.0$ ns, when the fuel-shell interface is close to a minimum, for shell thicknesses Δr from 24 to 27 μm , and intensities I of 0.75 to 1.0 times nominal. A straight line was fit to each set of values of R_{fs} for a given I . The value of shell thickness Δr as a function of intensity that results in an R_{fs} of 49 μm at $t = 2.0$ ns was determined from these fits by linear regression. The resulting equation for Δr in microns as a function of intensity is given by

$$\Delta r = 6.4 + 29.6 I - 9.0 I^2, \quad (1)$$

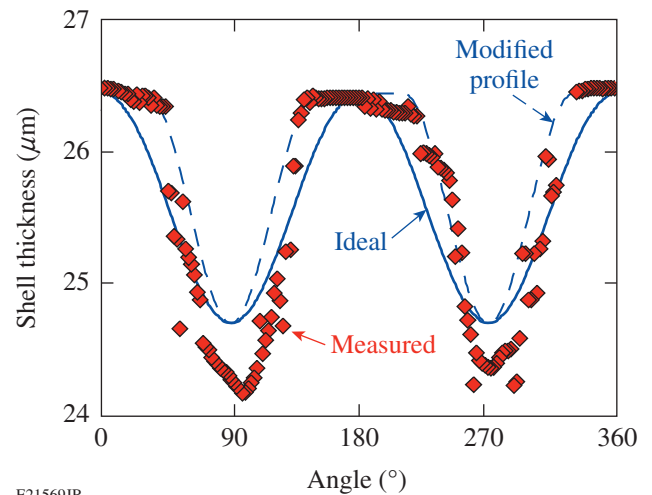
where I is in units of the nominal intensity. The lowest even mode intensity perturbation that could result from PD illumination is the second Legendre mode, i.e. $\ell = 2$. By restricting the perturbation to this first even Legendre mode, the intensity is given by

$$I(\theta) = I_0 \left[1 + \frac{i_2}{2} (3 \cos^2 \theta - 1) \right] / (1 + i_2), \quad (2)$$

where I_0 is the intensity at $\theta = 0$ and i_2 is the amplitude of the $\ell = 2$ mode. When Eq. (2) is substituted into Eq. (1), the ideal shell thickness profile is determined for this intensity profile.

The shimmed shells used in the experiments described in this article were manufactured by precision machining at the General Atomics (GA) Target Facility.¹² The ideal target profile was chosen by assuming that the average intensity profile was 10% prolate ($i_2 = +0.1$)—a magnitude and sign likely to result from PD illumination but otherwise an arbitrary choice. To

accomplish this process on a lathe using a single mounting direction, it was decided to avoid machining the shells near the poles (also the rotation axis of the lathe), avoiding errors in alignment introduced by switching the mounting direction of the target from one pole to the other. This leaves a region of constant shell thickness near the poles. Figure 135.14 shows the ideal profile, a modified profile that avoids the need to machine the poles, and an actual measured profile for one GA-machined shell. The modified profile is arrived at from the ideal profile by setting Δr equal to a constant from 0° to 30° and then using $\Delta r = \Delta r(\theta')$, where $\theta' = (\theta - 30^\circ) \times 1.5$ for $30^\circ \leq \theta \leq 90^\circ$. The initial mean shell thickness for this shell was 26.5 μm , so all values of the calculated profiles were shifted by 0.5 μm , and the machining was performed with respect to this thinner profile. The measured profile is close to the modified profile. Machining errors were kept to ~ 0.5 μm from the desired thickness. Three such targets were used in OMEGA experiments, and the results were compared to targets that were manufactured in an identical fashion at GA but did not undergo machining.



E21569JR

Figure 135.14

Measured shimmed shell thickness as a function of polar angle compared to the ideal profile and modified profile that avoids the need to machine near the poles.

The experiments were performed on OMEGA in the polar-drive configuration, where 40 of the 60 OMEGA beams are used to illuminate the target.⁵ The experiments were performed with 14 kJ of UV light (351 nm) using an ~ 3 -ns-duration, triple-picket pulse shape,⁷ designed to keep the target on a low adiabat, obtaining a high convergence ratio (CR, the ratio of the initial fuel-shell radius to final fuel-shell radius). CR's of ~ 19 were calculated for these experiments. The OMEGA laser

beams were smoothed using 0.5-THz-bandwidth smoothing by spectral dispersion (SSD),¹³ with polarization smoothing.¹⁴ The beam profiles were shaped using distributed phase plates (DPP's), resulting in a super-Gaussian beam shape given by $I/I_0 = \exp[-(r/r_0)^n]$ with $r_0 = 308 \mu\text{m}$ and $n = 3.66$ (Ref. 15). Beam pointing was chosen by using the modified capsule thickness profile as input to a series of *DRACO* 2-D hydrocode simulations¹⁶ with varying beam pointing. Beam offset is used to quantify beam pointing, with the magnitude being the distance from beam center to target center, perpendicular to the beam propagation direction, and with a positive offset meaning toward the equator of the PD axis.⁵ The pointing chosen (0-, 120-, and 140- μm offsets for rings 1, 2, and 3, respectively) resulted in the most-symmetric implosion in the simulations. This beam offset case is less than the case previously found for spherically symmetric shells with polar drive described in Marshall *et al.*⁶ (90-, 150-, and 150- μm offsets for rings 1, 2, and 3, respectively). The beams were precision pointed to an accuracy of $\sim 8 \mu\text{m}$ to these ideal offset locations using the method described in Ref. 15.

The time-dependent shapes of the imploding shells were measured with framed x-ray backlighting, using a 6- μm -thick Ti foil illuminated by 8 of the 20 remaining OMEGA beams. The beams were overlapped onto the foil, four on each side, defocused to a diameter of 0.7 mm. The foil was thin enough (6 μm) to be nearly transparent to the principal Ti-emitting line at 4.75 keV ($\text{He}\alpha$), effectively doubling the backlighter brightness. The backlighter was placed on the opposite side of the target from a high-speed framing camera¹⁷ having four strips, each timed to capture an array of images from 10- μm -diam pinholes, with a magnification of 6, spaced so that the separation in time of each image was 30 ps. The view of the target was 11° from the equator of the polar-drive axis, where the shapes of the observed radiographs were almost the same as at the equator (within $\sim 2\%$ for pure ℓ modes at this angle, see Ref. 5). Absolute frame times were determined from observation of the backlighter onset on the first strip, from the measured strip-to-strip delay, and from the image-to-image time delay on a strip. An absolute time accuracy of ~ 50 ps was obtained with a frame-to-frame time accuracy of ~ 15 ps. As described in Ref. 6, the recorded images were corrected for both film sensitivity and backlighter intensity variation as a function of position and are presented as the optical depth of the radiographed plasma as a function of position. Figure 135.15 shows sample radiographs of a spherical shell and two shimmed shells. The two shimmed shell cases are shown to demonstrate repeatability. The times are from the end of the laser pulse (~ 3.0 ns) to a time just before shell stagnation (~ 3.5 ns). As can be seen from the images, the

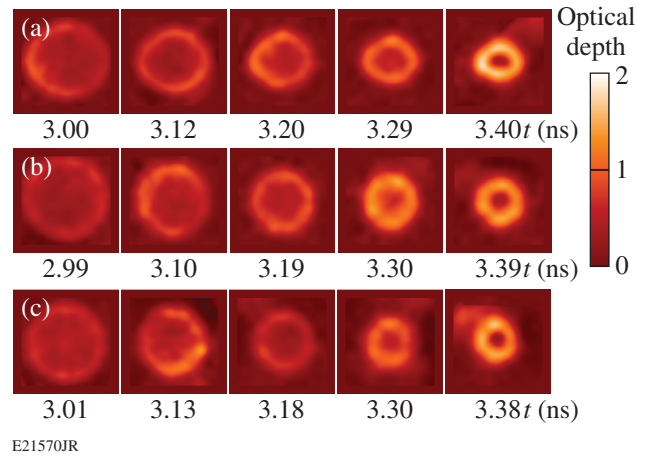


Figure 135.15

Sample radiographs of $500 \times 500\text{-}\mu\text{m}$ regions centered on the imploding plasma shell for (a) a spherical shell and [(b,c)] two shimmed shells, all imploded with the same beam-pointing condition.

shimmed shells implode with a more spherical shape for this beam pointing.

The shapes of the imploding plasmas are quantified by fitting the positions of the observed peak optical depth as a function of angle to the PD axis to a Legendre polynomial. The shape of the plasma is well measured at times corresponding to CR's of ~ 7 or less. At later times (higher CR's) self-emission obscures the backlighter. Figure 135.16 shows sample fits to both measured and simulated radiographs for a spherical shell [Figs. 135.16(a) and 135.16(b)] and a shimmed shell [Figs. 135.16(c) and 135.16(d)], both at the latest time measured. The simulated radiographs are determined from *DRACO* simulations. The shell shape is included in the shimmed-target simulations by a Legendre-mode decomposition up to mode 10 of the measured shell thickness. The simulations were post-processed by the code *Spect3D*,¹⁸ which takes into account radiation transport, spatial blurring ($\sim 15 \mu\text{m}$), and integration over the frame time (30 ps). Mode amplitudes (normalized to the average radius) of the fits at all measured times for the two most significant modes $\ell = 2$ and $\ell = 4$ modes (i.e., a_2 and a_4) are shown for both the spherical shell [Fig. 135.16(e)] and the shimmed shell [Fig. 135.16(f)]. The spherical shell develops a significant negative a_2 ($\sim -15\%$) late in time indicative of an oblate shape. The $\ell = 4$ mode is significant and positive ($\sim +5\%$). The shimmed shell target obtains a more nearly spherical shape with a_2 and a_4 being $\lesssim 2\%$ to 3% for all times measured. The amplitudes determined from the simulations are close to those observed. For the spherical target case [Fig. 135.16(e)], both the sign and magnitude of a_2 from the simulation match the observations, whereas the magnitude of a_4 is overpredicted

compared to observations. This is also true for the shimmed target [Fig. 135.16(f)], where both observations and simulations show a small a_2 but the simulation predicts a positive a_4 of $\sim 5\%$ to 10% . This may indicate a difference in the actual and predicted distribution of material in the plasma at that time. Nevertheless, the shimmed target obtains the most symmetric shape in both experiment and simulation for these cases.

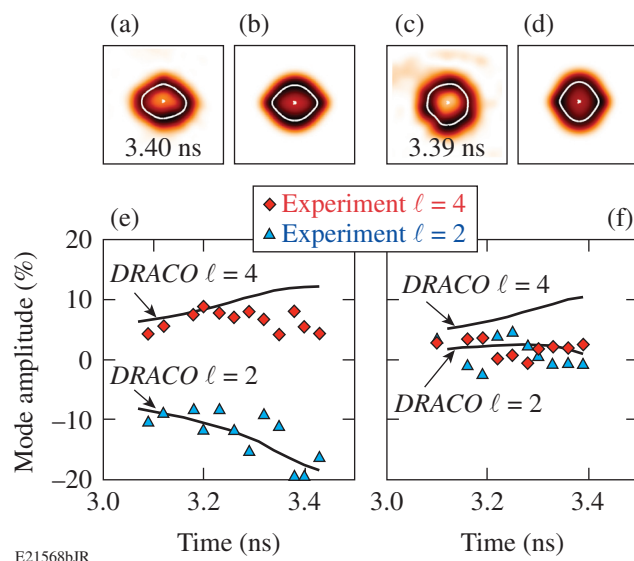


Figure 135.16

Fits to (a) measured and (b) simulated radiographs for a spherical shell, and fits to (c) measured and (d) simulated radiographs for a shimmed shell, at the indicated times. All regions are $500 \times 500 \mu\text{m}$. The $\ell = 2$ and $\ell = 4$ components of the fits to the measured radiographs are shown in (e) and (f) along with values determined from the simulations.

These results show that a shimmed target can improve the symmetry of a polar-driven imploding shell but taken alone do not demonstrate the benefit of using shimmed shells over just beam repointing to control this shape. The combined benefit is more aptly demonstrated by comparing the symmetry of spherical targets imploded by polar-drive beam pointing, chosen to give the best low-mode symmetry ($a_2 \approx 0$), with the shimmed target result of Fig. 135.16. Figure 135.17 shows the modal fit to a radiograph of a spherical shell imploded with a beam repointing of 90-, 133-, and 133- μm offsets for Rings 1, 2, and 3, respectively, (all other conditions the same) compared to the shimmed shell with the beam pointing given above at ~ 100 ps before stagnation (3.4 ns) and with nearly equal average radii ($\sim 70 \mu\text{m}$). Note that for the spherical target $a_2 \approx 0$, while $a_4 \approx +16\%$. The plasma exhibits a “diamond-like” shape from this significant positive $\ell = 4$ mode. In contrast, a_2 and a_4 are both small ($\leq 2\%$) for the shimmed target, demonstrating the

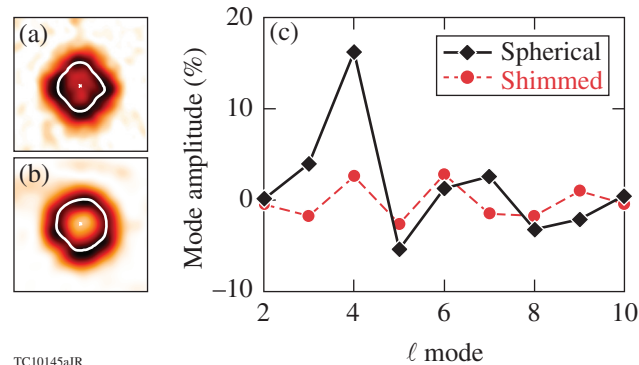


Figure 135.17

Fits to radiographs of (a) a spherical target with optimum pointing for the spherical target (see text), and (b) a shimmed target with the pointing used for the shimmed target experiments (see text). Both radiographs are of $400 \times 400\text{-}\mu\text{m}$ regions just before stagnation of the shell. (c) Mode amplitudes from Legendre polynomial fits to these shapes

combined benefit of beam repointing and target shimming in controlling the shape of the polar-driven implosion.

As demonstrated by these experiments, target shimming can increase the low-mode symmetry over beam repointing alone. Given the need to control the shape of PD implosions on the NIF, and the anticipated benefit of shimming to increase the ignition margin, these results indicate that further research into methods to shape the DT encapsulating shell, and/or the DT layer itself should be undertaken. Indirectly driven implosions may also benefit from using a shimmed target, emphasizing the importance of this method.

ACKNOWLEDGMENT

The authors acknowledge the support of the staff at the University of Rochester’s Laboratory for Laser Energetics. This work was supported by the U.S. Department of Energy, Office of Inertial Confinement Fusion under Cooperative Agreement No. DE-FC52-08NA28302, the University of Rochester, and the New York State Energy Research and Development Authority.

REFERENCES

1. S. Skupsky, J. A. Marozas, R. S. Craxton, R. Betti, T. J. B. Collins, J. A. Delettrez, V. N. Goncharov, P. W. McKenty, P. B. Radha, T. R. Boehly, J. P. Knauer, F. J. Marshall, D. R. Harding, J. D. Kilkenny, D. D. Meyerhofer, T. C. Sangster, and R. L. McCrory, *Phys. Plasmas* **11**, 2763 (2004).
2. G. H. Miller, E. I. Moses, and C. R. Wuest, *Opt. Eng.* **43**, 2841 (2004).
3. T. R. Boehly, D. L. Brown, R. S. Craxton, R. L. Keck, J. P. Knauer, J. H. Kelly, T. J. Kessler, S. A. Kumpan, S. J. Loucks, S. A. Letzring, F. J. Marshall, R. L. McCrory, S. F. B. Morse, W. Seka, J. M. Soures, and C. P. Verdon, *Opt. Commun.* **133**, 495 (1997).

4. R. S. Craxton, F. J. Marshall, M. J. Bonino, R. Epstein, P. W. McKenty, S. Skupsky, J. A. Delettrez, I. V. Igumenshchev, D. W. Jacobs-Perkins, J. P. Knauer, J. A. Marozas, P. B. Radha, and W. Seka, *Phys. Plasmas* **12**, 056304 (2005).
5. F. J. Marshall, R. S. Craxton, M. J. Bonino, R. Epstein, V. Yu. Glebov, D. Jacobs-Perkins, J. P. Knauer, J. A. Marozas, P. W. McKenty, S. G. Noyes, P. B. Radha, W. Seka, S. Skupsky, and V. A. Smalyuk, *J. Phys. IV France* **133**, 153 (2006).
6. F. J. Marshall, P. W. McKenty, J. A. Delettrez, R. Epstein, J. P. Knauer, V. A. Smalyuk, J. A. Frenje, C. K. Li, R. D. Petrasso, F. H. Séguin, and R. C. Mancini, *Phys. Rev. Lett.* **102**, 185004 (2009).
7. P. B. Radha, J. A. Marozas, F. J. Marshall, A. Shvydky, T. J. B. Collins, V. N. Goncharov, R. L. McCrory, P. W. McKenty, D. D. Meyerhofer, T. C. Sangster, and S. Skupsky, *Phys. Plasmas* **19**, 082704 (2012).
8. J. A. Marozas, F. J. Marshall, R. S. Craxton, I. V. Igumenshchev, S. Skupsky, M. J. Bonino, T. J. B. Collins, R. Epstein, V. Yu. Glebov, D. Jacobs-Perkins, J. P. Knauer, R. L. McCrory, P. W. McKenty, D. D. Meyerhofer, S. G. Noyes, P. B. Radha, T. C. Sangster, W. Seka, and V. A. Smalyuk, *Phys. Plasmas* **13**, 056311 (2006).
9. T. J. B. Collins, J. A. Marozas, K. S. Anderson, R. Betti, R. S. Craxton, J. A. Delettrez, V. N. Goncharov, D. R. Harding, F. J. Marshall, R. L. McCrory, D. D. Meyerhofer, P. W. McKenty, P. B. Radha, A. Shvydky, S. Skupsky, and J. D. Zuegel, *Phys. Plasmas* **19**, 056308 (2012).
10. J. D. Lindl *et al.*, *Phys. Plasmas* **11**, 339 (2004).
11. J. Delettrez, R. Epstein, M. C. Richardson, P. A. Jaanimagi, and B. L. Henke, *Phys. Rev. A* **36**, 3926 (1987).
12. General Atomics, San Diego, CA 92121-1122.
13. S. Skupsky, R. W. Short, T. Kessler, R. S. Craxton, S. Letzring, and J. M. Soures, *J. Appl. Phys.* **66**, 3456 (1989).
14. T. R. Boehly, V. A. Smalyuk, D. D. Meyerhofer, J. P. Knauer, D. K. Bradley, R. S. Craxton, M. J. Guardalben, S. Skupsky, and T. J. Kessler, *J. Appl. Phys.* **85**, 3444 (1999).
15. R. A. Forties and F. J. Marshall, *Rev. Sci. Instrum.* **76**, 073505 (2005).
16. P. B. Radha, V. N. Goncharov, T. J. B. Collins, J. A. Delettrez, Y. Elbaz, V. Yu. Glebov, R. L. Keck, D. E. Keller, J. P. Knauer, J. A. Marozas, F. J. Marshall, P. W. McKenty, D. D. Meyerhofer, S. P. Regan, T. C. Sangster, D. Shvarts, S. Skupsky, Y. Srebro, R. P. J. Town, and C. Stoeckl, *Phys. Plasmas* **12**, 032702 (2005).
17. D. K. Bradley *et al.*, *Rev. Sci. Instrum.* **66**, 716 (1995).
18. J. J. MacFarlane *et al.*, *High Energy Density Phys.* **3**, 181 (2007).